Phase Stability and Vibrational Properties of Iron-Bearing Carbonates at High Pressure

Chaoshuai Zhao, Liangxu Xu, Weibin Gui and Jin Liu *

Center for High Pressure Science and Technology Advanced Research (HPSTAR), Beijing 100094, China; chaoshuai.zhao@hpstar.ac.cn (C.Z.); liangxu.xu@hpstar.ac.cn (L.X.); guiweibin@outlook.com (W.G.)
* Correspondence: jin.liu@hpstar.ac.cn

check for updates

Abstract: The spin transition of iron can greatly affect the stability and various physical properties of iron-bearing carbonates at high pressure. Here, we reported laser Raman measurements on iron-bearing dolomite and siderite at high pressure and room temperature. Raman modes of siderite $FeCO_3$ were investigated up to 75 GPa in the helium (He) pressure medium and up to 82 GPa in the NaCl pressure medium, respectively. We found that the electronic spin-paring transition of iron in siderite occurred sharply at 42–44 GPa, consistent with that in the neon (Ne) pressure medium in our previous study. This indicated that the improved hydrostaticity from Ne to He had minimal effects on the spin transition pressure. Remarkably, the spin crossover of siderite was broadened to 38–48 GPa in the NaCl pressure medium, due to the large deviatoric stress in the sample chamber. In addition, Raman modes of iron-bearing dolomite $Ca_{1.02}Mg_{0.76}Fe_{0.20}Mn_{0.02}(CO_3)_2$ were explored up to 58 GPa by using argon as a pressure medium. The sample underwent phase transitions from dolomite-I to -Ib phase at ~8 GPa, and then to -II at ~15 and -IIIb phase at 36 GPa, while no spin transition was observed in iron-bearing dolomite up to 58 GPa. The incorporation of $FeCO_3$ by 20 mol% appeared to marginally decrease the onset pressures of the three phase transitions aforementioned for pure dolomite. At 55–58 GPa, the ν_1 mode shifted to a lower frequency at ~1186 cm^{-1}, which was likely associated with the 3 + 1 coordination in dolomite-IIIb. These results shed new insights into the nature of iron-bearing carbonates at high pressure.

Keywords: iron-bearing carbonate; high pressure; Raman spectroscopy; spin transition; stability

1. Introduction

Carbon mainly exists as accessory minerals (e.g., carbonates, diamond, graphite, and carbides) in the deep mantle due to its relatively low solubility in silicates [1]. Carbonates are considered to be one of the most important carbon carriers from the crust to deep mantle [2–4]. Given carbonate inclusions in ultra-deep diamonds originating from the deep mantle, carbonates can descend to the Earth's deep interior [5,6]. The presence of carbonates may dramatically affect the physical and chemical properties (e.g., melting, viscosity, electrical conductivity, thermal conductivity, and elasticity) of the deep mantle [7–9]. More importantly, knowledge of the stability of carbonates is indispensable to interpret the deep carbon cycle.

Iron plays a fundamental role in the behavior of carbonates at extreme conditions, relevant to the Earth's lower mantle [7,10]. In particular, iron substitution can greatly change the thermodynamic stability of $MgCO_3$ and other mantle phases at high pressure and high temperature [11–14]. Siderite is considered to be more stable than magnesite due to Fe^{2+} in the low-spin (LS) state with a radius smaller than Mg^{2+}. It could be preserved in relatively cold subducting slabs down to the lower mantle [15–18]. Most of the previous studies about iron-bearing carbonates have concentrated on the spin transition of iron in $FeCO_3$ [10,17–23]. The onset pressure of spin transition, as well as the width of spin crossover,

appear to be greatly affected by hydrostatic conditions of the sample chamber. Intriguingly, it is still unclear how the helium or NaCl pressure medium influences the behavior of siderite at high pressure.

Iron-bearing dolomite has also been suggested to enter the Earth's interior through subduction slabs. It adopts a rhombohedral structure (space group $R\bar{3}$) with alternating layers of CaO_6 and MgO_6 octahedra stacked along the *c*-axis at ambient conditions [24]. The stability of dolomite has been investigated at lower mantle conditions and most of the previous studies have concentrated on its phase stability and vibrational properties by using a battery of experimental methods (e.g., X-ray diffraction, Raman, and infrared) [24–30]. Further investigation is needed to determine how iron substitution affects the nature of dolomite at a high pressure.

In the present work, we collected the high-pressure Raman spectra of siderite $FeCO_3$ and iron-bearing dolomite $Ca_{1.02}Mg_{0.76}Fe_{0.20}Mn_{0.02}(CO_3)_2$ natural samples at high pressure in diamond anvil cells (DACs). The siderite sample was compressed in the He pressure medium to 75 GPa and in the NaCl pressure medium to 82 GPa, respectively. The use of He and NaCl allowed us to better understand how hydrostatic and non-hydrostatic conditions affected the stability and spin transition of $FeCO_3$ at high pressures. As compared with our previous results, there was a negligible impact on the spin transition in $FeCO_3$ between Ne and He pressure-transmitting media. We also carried out laser Raman measurements on iron-bearing dolomite at high pressure up to 58 GPa at room temperature by using argon as a pressure-transmitting medium. In this study, we found that there was no spin transition that occurred in the iron-bearing dolomite sample. These results improved the knowledge about phase stability and vibrational properties of iron-bearing carbonates at high pressure.

2. Experimental Methods

2.1. Sample Characterization

The starting materials were natural siderite $Fe_{0.998}Mn_{0.002}CO_3$ single-crystal samples obtained from the mineralogical collection of the Department of Mineral Sciences, Smithsonian Institution (collection no. NMNH R11313). The chemical composition of the siderite sample contained less than 0.2 mol% of $MnCO_3$, which was determined using electron microprobe analyses (JEOL JXA-8200, The University of Texas at Austin, USA). For simplicity, we neglected the minor impurity, and thus referred to the composition of the sample as $FeCO_3$ thereinafter. $FeCO_3$ has the crystal structure of calcite ($CaCO_3$). Single-crystal X-ray diffraction (XRD) patterns confirmed the $R\bar{3}c$ structure with lattice parameters $a = 4.6909(5)$ Å and $c = 15.3687(49)$ Å for $FeCO_3$ under ambient conditions, in good agreement with previous studies [31]. For the dolomite sample, based on electron microprobe analyses (JEOL JXA-8230, Northwest University, China), the chemical composition was $Ca_{1.02}Mg_{0.76}Fe_{0.20}Mn_{0.02}(CO_3)_2$.

2.2. High-Pressure Raman Spectroscopy

High-pressure Raman spectra of $FeCO_3$ were collected by using a Renishaw Raman spectroscopy (RM1000, Center for High Pressure Science and Technology Advanced Research, China) excited by a 532 nm wavelength of an Ar^+ laser. The spectral resolution was about 2 cm^{-1} with the holographic diffraction grating of 1800 lines/mm. High pressures were produced by a symmetric diamond anvil cell (DAC) mounted with a pair of 200 μm diamond anvils. A ~30 μm thickness of pre-indented tungsten gasket with a 120 μm hole was used as a sample chamber. Together with two ruby spheres, a platelet of single-crystal $FeCO_3$ was loaded into the sample chamber using He as a pressure medium. The use of He can maintain the hydrostatic conditions at 50 GPa [32], and thus avoid the influence of deviatoric stress. For more detailed experimental information, one can refer to our previous study [33]. Additionally, the Raman spectra of iron-bearing dolomite were collected by using an eXcelon digital CCD spectroscopy system (PIXIS 400, Princeton Instruments co., USA) coupled with an 1800 G/mm ruled grating with 532 nm blaze wavelength. It was equipped with a Coherent Verdi V2 laser with a wavelength of 532 nm. Pressure was determined by using multiple measurements of the ruby fluorescence before and after each experimental run in the He [34], NaCl, or argon pressure-transmitting

medium [35]. Raman spectra fitting was carried out using the software PeakFit v4.12 with the Voigt area method.

3. Results and Discussion

Raman spectra of siderite $FeCO_3$ and iron-bearing dolomite $Ca_{1.02}Mg_{0.76}Fe_{0.20}Mn_{0.02}(CO_3)_2$ were collected in varying pressure-transmitting media at high pressure and room temperature. Rhombohedral carbonates (e.g., siderite, calcite, magnesite, and dolomite) with the space group $R\bar{3}c$ or $R\bar{3}$ have two lattice modes (*T* and *L* modes) and four internal modes (in-plane bend internal (v_4), symmetric stretch internal (v_1), anti-symmetric stretch (v_3), and out-of-plane bend ($2v_2$) modes) [36]. At ambient conditions, the four Raman modes of *T*, *L*, v_4, and v_1 were collected in $FeCO_3$ and $Ca_{1.02}Mg_{0.76}Fe_{0.20}Mn_{0.02}(CO_3)_2$ from 100 to 1300 cm^{-1}. These Raman mode values are consistent with literature values [31,36,37].

3.1. Spin Transition of $FeCO_3$

Representative Raman spectra of siderite $FeCO_3$ at high pressure up to 75 GPa were observed, as shown in Figure 1, by using He as a pressure-transmitting medium. The inset in Figure 1 illustrates optical images of the single-crystal siderite in the DAC. The color of siderite platelet is colorless and transparent in the high-spin (HS) state. At 42 GPa, part of the crystallite changes from transparent to green and the spectral features of siderite changes significantly due to the spin transition of Fe^{2+} [18,38]. The emergence of *L'*, v_4', and v_1' modes was observed in nearly pure $FeCO_3$ at 42 GPa, suggesting coexistence of the two species with different unit-cell volumes that correspond to the HS and LS domains, respectively [20,39]. The v_1' mode that occurred at the left of the original v_1 mode provided strong evidence of the spin transition for iron-bearing carbonates [19,20,22,40]). The *L* and v_4 modes of $FeCO_3$ in the LS state jump to higher wavenumbers because of the reduced distance between the CO_3^{2-} groups and the cations, and the shortening of O-O distances, respectively [17,40]). Meanwhile, the v_1 mode shifts to lower wavenumbers from the HS to LS states, due to an increase in the C-O bond lengths across the spin transition [19,20,39,40]. The lengthening of the C-O bond and the contraction of the O-O distances were reported in the single-crystal XRD study across the spin transition by Lavina et al. (2010) [17].

The optical image of siderite completely changes to green at 44 GPa when the original *L*, v_4, and v_1 modes disappear. It turns into red above 50–55 GPa. The change of crystal color can be assigned to a significant increase in the overall optical absorption of siderite in the LS state. The green color of siderite comes from the absorption minima of the ^1A_g to $^1T_{1g}$ band, while the red color is due to the overlap of the crystal field band with the absorption edge [18]. The Raman spectra and optical images demonstrate that the electronic spin-paring of iron in $FeCO_3$ occurs sharply at 42–44 GPa by using the He pressure medium, comparable to using the Ne pressure medium [16,18,40], that is, the enhanced hydrostaticity from Ne to He has a neglected effect on the spin transition pressure. In contrast, we observed a broadened spin crossover with the same siderite sample using NaCl as a pressure medium (Figure 2). Between 38 and 48 GPa, a weak shoulder is assigned as the v_1' mode next to the initial v_1 mode. The obvious splitting of the v_1 mode at 41.5 and 44.8 GPa represents the mixed spin state of siderite. With further compression, the intensity of the two v_1 modes exchanges. The v_1 mode completely disappears at 48.4 GPa, indicating the loss of the HS state. Figure 3 shows the low-spin fraction of siderite as a function of pressure with the use of NaCl as a pressure-transmitting medium. The HS-LS fraction was determined on the basis of the ratio of the Raman peak areas between the v_1 and v_1' modes. The low-spin fraction changes dramatically from 38 to 48 GPa corresponding to the spin crossover of siderite. Moreover, compared to the use of He as a pressure medium, the onset pressure of spin transition is lowered by ~4 GPa using NaCl as a pressure medium. The same effect of non-hydrostatic stress has also been observed for high-pressure phase transitions of other minerals, e.g., barite $BaSO_4$ and rhodochrosite $MnCO_3$ [41,42].
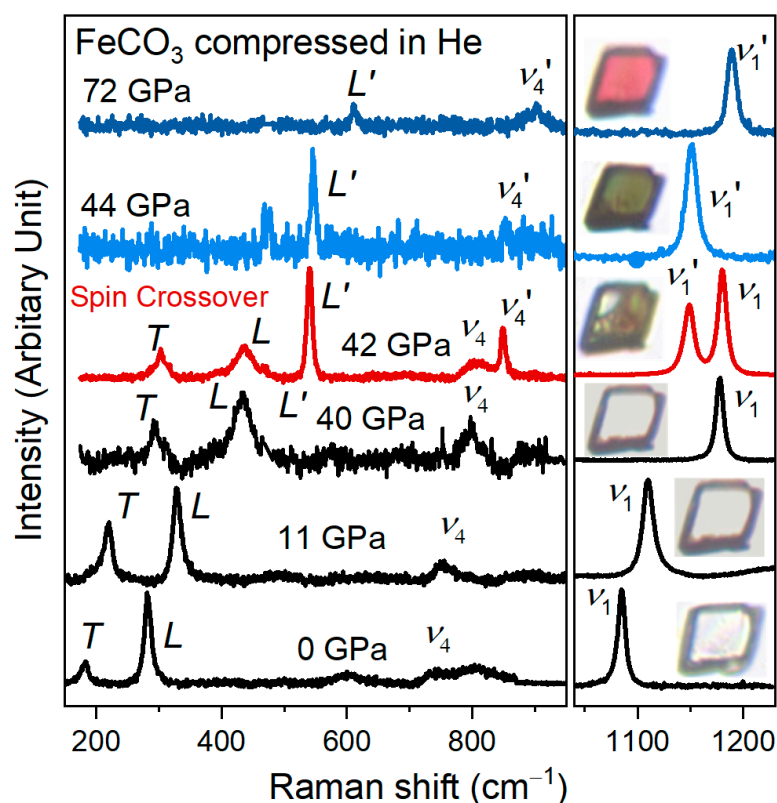
Figure 1. Representative Raman spectra of siderite $FeCO_3$ at high pressures. The Raman modes are labeled as T, L, v_4, and v_1 based on Rividi et al. (2010) [36]. The T, L, and v_4 modes were simultaneously enlarged to illustrate changes in Raman spectra of siderite. At 42 GPa, the splitting of L, v_4, and v_1 modes into L', v_4', and v_1' indicates the occurrence of spin transition of Fe^{2+} in siderite. Insets, the color evolution of siderite sample captured through optical microscope images.
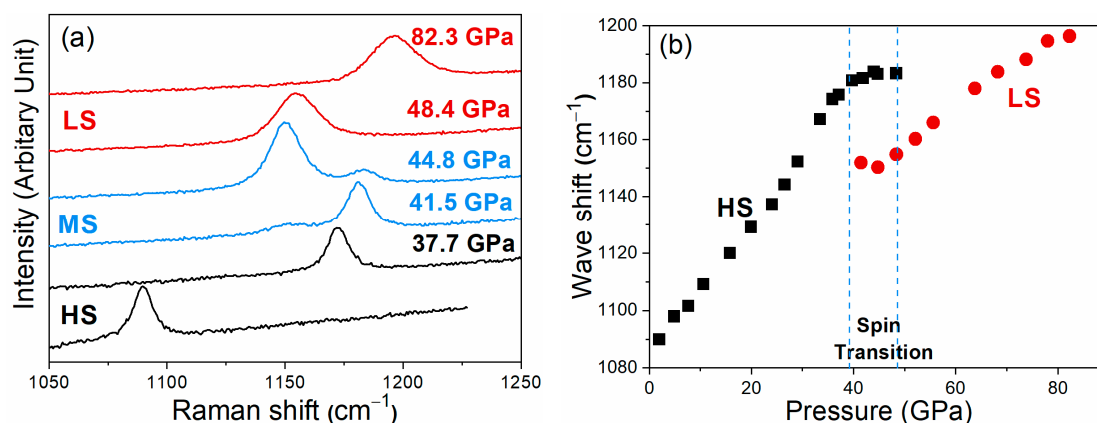

Figure 2. Representative Raman spectra (**a**) and Raman shifts (**b**) of v_1 mode of siderite using NaCl as a pressure-transmitting medium. A weak shoulder assigned as the v_1' mode near the initial v_1 mode was observed between 38 and 48 GPa. The v_1 and v_1' modes correspond to the high- and low-spin (HS and LS) states, respectively. The obvious split of v_1 mode at 41.5 and 44.8 GPa represents the mixture spin state of siderite. With the further increase of pressure, the intensity of two v_1 modes is exchanged. The v_1 mode completely disappears at 48.4 GPa, indicating the completion of spin transition. The two blue dashed lines represent the spin crossover of siderite.
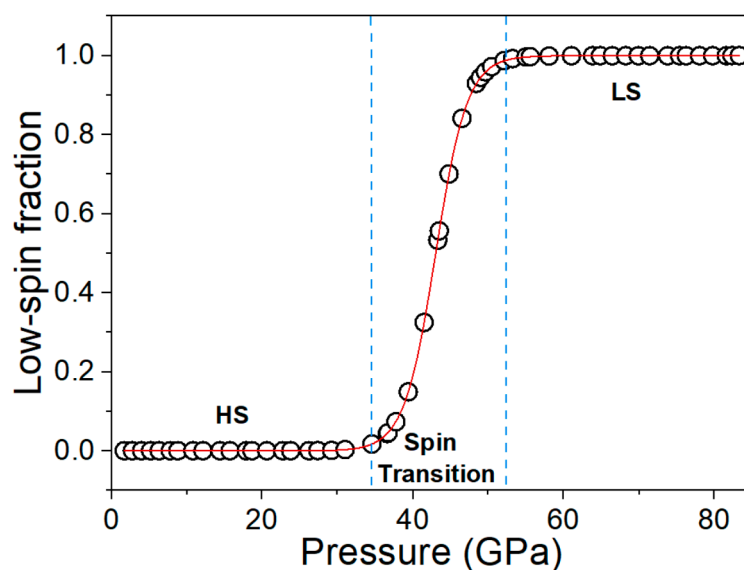
Figure 3. The low-spin fraction of siderite as a function of pressure with the use of NaCl as a pressure-transmitting medium. The low-spin fraction changes dramatically at around 38 to 48 GPa, corresponding to the spin crossover of siderite.

The literature data on the spin crossover of $(Mg,Fe)CO_3$ are summarized in Figure 4 and Table 1. In order to accurately estimate the effects of $FeCO_3$ content on the spin crossover of $(Mg,Fe)CO_3$, the datasets are grouped in the two categories, as shown in Figure 4, i.e., hydrostatic/quasi-hydrostatic (Ne or Ne as a pressure medium) and non-hydrostatic conditions (silicone oil, argon, NaCl, or no pressure medium). By considering the uncertainty induced by varying methods (e.g., Raman, XRD), the spin transition pressure of $(Mg,Fe)CO_3$ is not sensitive to $FeCO_3$ content under hydrostatic/quasi-hydrostatic conditions [10]. It can be explained by the relatively large Fe^{2+} to Fe^{2+} distance separated by $(CO_3)^{2-}$ units in $(Mg,Fe)CO_3$ [20].
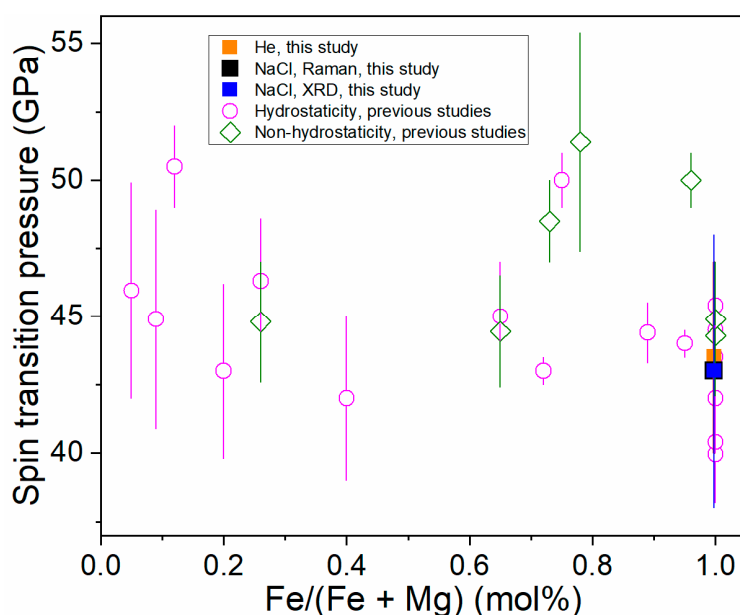

Figure 4. The spin crossover of magnesite-siderite solid solutions with increasing iron content under hydrostatic and non-hydrostatic pressure conditions. The composition of $(Mg,Fe)CO_3$ is the same as in Table 1. The black square is enlarged to differ from the overlapped blue square.

Table 1. Spin transition of (Mg,Fe)CO$_3$.

Composition	PTM	Transition P	Method	Reference
Fe$_{0.998}$Mn$_{0.002}$CO$_3$	He	42–44	Raman	This study
Fe$_{0.998}$Mn$_{0.002}$CO$_3$	NaCl	40–47	Raman	This study
Fe$_{0.998}$Mn$_{0.002}$CO$_3$	NaCl	38–48	XRD	This study
FeCO$_3$	Ne	44.6-46.2	XRD	[43]
FeCO$_3$	n.a.	~40	DFT, ISS	[44]
FeCO$_3$	Ne	40.0–40.8	X-ray Raman	[23]
FeCO$_3$	Argon	42.1–46.5	X-ray Raman	[23]
FeCO$_3$	Argon	42.8–47	Raman	[40]
FeCO$_3$	n.a.	45–50	DFT	[45]
FeCO$_3$	Ne	40–47	Raman	[19]
FeCO$_3$	Ne	~42	XRD	[16]
FeCO$_3$	Ne	40–47	Raman	[22]
FeCO$_3$	Ne	44–45	XRD	[17]
Fe$_{0.96}$Mn$_{0.04}$CO$_3$	Argon	~50	XES	[46]
Fe$_{0.96}$Mn$_{0.04}$CO$_3$	None	~50	XES	[46]
Fe$_{0.95}$Mn$_{0.05}$CO$_3$	Ne	43–45	UV-VIS	[18]
Fe$_{0.89}$Mn$_{0.07}$Mg$_{0.03}$Ca$_{0.01}$CO$_3$	Ne	43.3–45.5	Raman	[40]
(Fe$_{0.78}$Mg$_{0.22}$)CO$_3$	Silicone oil	47.7–55.4	Raman	[47]
(Fe$_{0.75}$Mg$_{0.25}$)CO$_3$	none	50	XRD	[48]
Fe$_{0.65}$Mg$_{0.33}$Mn$_{0.02}$CO$_3$	Ne	43–47	XRD	[10]
Fe$_{0.65}$Mg$_{0.33}$Mn$_{0.02}$CO$_3$	Ne	45	XRD	[20]
Fe$_{0.65}$Mg$_{0.33}$Mn$_{0.02}$CO$_3$	Ne	45	Raman	[20]
(Fe$_{0.73}$Mg$_{0.22}$Mn$_{0.05}$)CO$_3$	Argon	47–50	XRD	[21]
(Fe$_{0.72}$Mg$_{0.24}$Mn$_{0.03}$Ca$_{0.01}$)CO$_3$	Ne	~43	XRD	[38]
Fe$_{0.65}$Mg$_{0.35}$CO$_3$	Ne	42.4–46.5	BS, ISS	[7]
(Fe$_{0.5}$Mg$_{0.5}$)CO$_3$	n.a.	45–50	DFT	[45]
(Fe$_{0.26}$Mg$_{0.74}$)CO$_3$	Ne	44.0-48.5	XRD	[43]
(Fe$_{0.26}$Mg$_{0.74}$)CO$_3$	Argon	42.6–47.0	X-ray Raman	[23]
(Fe$_{0.167}$Mg$_{0.833}$)CO$_3$	n.a.	None	DFT	[49]
(Fe$_{0.125}$Mg$_{0.875}$)CO$_3$	n.a.	45–50	DFT	[45]
(Fe$_{0.09}$Mg$_{0.91}$)CO$_3$	Ne	41–49	Raman	[22]
(Fe$_{0.05}$Mg$_{0.95}$)CO$_3$	Ne	42–50	Raman	[22]

PTM, pressure-transmitting medium. The "none" and "n.a." in the column of PTM stand for experiments and calculations carried out without PTM.

Raman shifts of each mode in FeCO$_3$ can be linearly fitted as a function of pressure before and after the spin transition, respectively, when He is used as a pressure-transmitting medium (Figure 5 and Table 2). We note that the T mode might be too weak to be observed in the LS state. The pressure dependences of L and ν_1 modes are 3.65 and 2.28 cm^{-1}/GPa, respectively, in the HS state. These modes in the LS state decrease by ~40% to 2.41 and 1.38 cm^{-1}/GPa, respectively, indicating that siderite in the LS state is stiffer and less compressible than in the HS state. By comparison, the pressure dependences of Raman shifts ($d\nu/dP$) in FeCO$_3$ (denoted as "sid100") in this study are comparable to that in sid65 in the HS state [20]. However, the pressure dependence of Raman shifts of L', ν_4', and ν_1' in sid100 are about 48%, 69%, and 47% greater than that in sid65 in the LS state. This is consistent with the observations that the bulk modulus of sid65 is higher than that of sid100 in the LS state at a given pressure [16,20]. We note that the discrepancy in the pressure dependence of Raman shifts between this study and Farsang et al. (2018) [31] may be related to the use of different pressure media and the pressure range of Raman spectroscopic measurements.
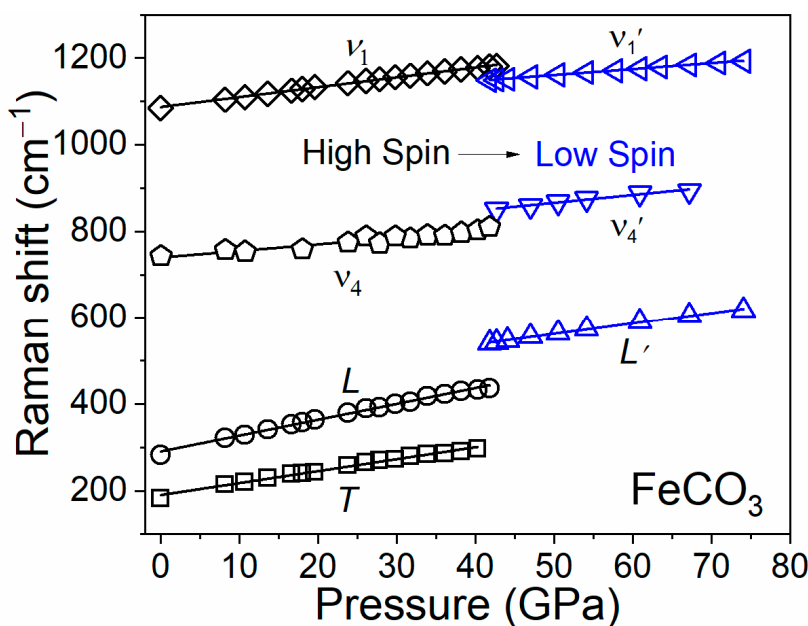
Figure 5. Raman shifts of siderite at high pressures using He as a pressure-transmitting medium. Solid lines represent linear fits in the HS (black) and LS (blue) states, respectively. Among all four modes, the *T* mode was not observed in Raman spectra of siderite in the LS state. Error bars within symbols are not shown for clarity.

Table 2. Vibrational parameters of siderite at high pressures.

Raman	Sid100 [a] (He)		Sid98 [b] (ME)		Sid89 [c] (Ne)	Sid100 [d] (Ne)		Sid76 [e] (Silicone oil)	Sid65 [f] (Ne)	
modes	$d\nu_i/dP$	γ_i	$d\nu_i/dP$	γ_i	$d\nu_i/dP$	$d\nu_i/dP$	γ_i[g]	$d\nu_i/dP$	$d\nu_i/dP$	γ_i
T (HS)	2.75(8)	1.75(7)	3.98(9)	2.54	-	2.51	1.18	-	2.51(1)	1.96(3)
L (HS)	3.65(7)	1.50(4)	4.52(5)	1.86	-	3.82	1.16	3.74	3.64(18)	1.87(3)
ν_4 (HS)	1.53(13)	0.24(2)	2.4(2)	0.38	-	1.37	0.21	-	1.49(6)	0.41(1)
ν_1 (HS)	2.28(3)	0.24(1)	2.60(7)	0.28	2.2(1)	2.17	0.22	2.20	2.17(7)	0.39(1)
T (LS)	-	-	-	-	-	-	-	-	1.86(16)	1.69(3)
L (LS)	2.42(7)	0.75(3)	-	-	-	2.68	0.72	-	1.64(17)	1.08(2)
ν_4 (LS)	1.81(13)	0.36(1)	-	-	-	1.86	0.32	-	1.07(8)	0.44(1)
ν_1 (LS)	1.38(2)	0.20(1)	-	-	1.5(1)	1.6	0.21	-	0.94(9)	0.30(1)

[a] Sid100, $(Fe_{0.998}Mn_{0.002})CO_3$, this study. The measured initial frequencies of Raman modes for HS and LS of siderite at 0 and 44 GPa are chosen to retrieve the mode Grüneisen parameters γ_i, respectively. The bulk moduli K_0 set as 116 GPa for HS and 169 GPa for LS with K'_0 fixed to 4 was used to derive the mode Grüneisen parameters γ_i of $FeCO_3$. [b] Sid98, $Fe_{0.98}Mg_{0.01}Mn_{0.01}CO_3$ [31]; [c] Sid89, $Fe_{0.89}Mn_{0.07}Mg_{0.03}Ca_{0.01}CO_3$ [40]; [d] Sid100, $FeCO_3$ [19]; [e] Sid76, $Fe_{0.76}Mn_{0.15}Mg_{0.09}Ca_{0.01}CO_3$ [39]; [f] Sid65, $Fe_{0.65}Mg_{0.33}Mn_{0.02}CO_3$ [20]; [g] γ_i, mean mode Grüneisen parameters; ME, Methanol and ethanol (4:1); $d\nu_i/dP$ in the unit of cm^{-1}/GPa.

Mode Grüneisen parameters provide important information about the relative contributions of each vibration to the thermochemical properties [50]. Combined with XRD and Raman results from previous work and this study, the mode Grüneisen parameters (γ_i) were derived according to the equation as follows:

$$\gamma_i = -\frac{d \ln \nu_i}{d \ln V} = \frac{K_T}{\nu}\left(\frac{d\nu_i}{dP}\right) \tag{1}$$

where ν_0, V, P, and K_T are frequency at ambient conditions in the unit of cm^{-1}, unit cell volume in the unit of Å^3, pressure in the unit of GPa, and isothermal bulk model in the unit of GPa, respectively.

On the basis of the Raman shifts of each mode in this study and the equation of state reported by Liu et al. (2015) [16], the mode Grüneisen parameters (γ_i) of sid100 in the HS and LS states were derived (Table 2). The γ_i values for L, ν_4, and ν_1 modes are 1.50, 0.24, and 0.24, respectively, in the

HS state, and change to 0.75, 0.36, and 0.20, respectively, in the LS state. The γ_i values of the L and ν_1 modes decrease by approximate 50% and 17%, while that of the ν_4 mode increases by 50% across the spin transition of iron in siderite, which should be attributed to the shrink of Fe-O octahedra [19,20]. By comparison, the mode Grüneisen parameters show a large difference among different studies, especially for T and L modes in the HS state, which are likely associated with pressure medium and compositional effects on the pressure dependence of Raman shifts. On the other hand, the γ_i values in the LS state are consistent with that in sid100 reported by Cerantola et al. (2015) [19], likely due to the similar chemical composition and compression environment.

3.2. Phase Transitions of Iron-Bearing Dolomite at High Pressure

Iron-bearing dolomite undergoes a series of phase transitions at the pressure range of this study (Figures 6 and 7 and Table 3). The splitting of a low frequency mode around 201 cm^{-1} was observed at 7.8 GPa, which indicates the occurrence of dolomite-Ib phase [25,26]. Moreover, the splitting of Raman mode at around 750 cm^{-1} and the several new Raman peaks observed at the low frequency of 200−600 cm^{-1} at 14.8 GPa are assigned as the onset of the dolomite-II phase. These Raman modes further split at ~36.0 GPa, together with a weak shoulder in ν_1 mode (shown as the black arrow in Figure 6), indicating the occurrence of dolomite-III phase. On the basis of the previous XRD studies, the dolomite-III is assigned as dolomite-IIIb for iron-rich dolomite, instead of dolomite-IIIc [29]. Given our work and previous studies on iron-bearing dolomite with varying iron contents at high pressure (Figure 7 and Table 3), we found that the onset pressure of phase transitions of dolomite-I to -Ib, -II, and -IIIb phases were almost insensitive with the iron content at the expense of the tilting of the CO$_3$ groups [24−26]. It should be mentioned that the phase transitions of iron-bearing dolomite are 2−4 GPa lower than that of iron-free dolomite CaMg(CO$_3$)$_2$ [25,28]. This means that the incorporation of iron (even though there is minimal iron) into pure dolomite endmember may decrease the onset phase transition of dolomite, likely due to the fact that iron substitution changes the ordered atom arrange of dolomite.
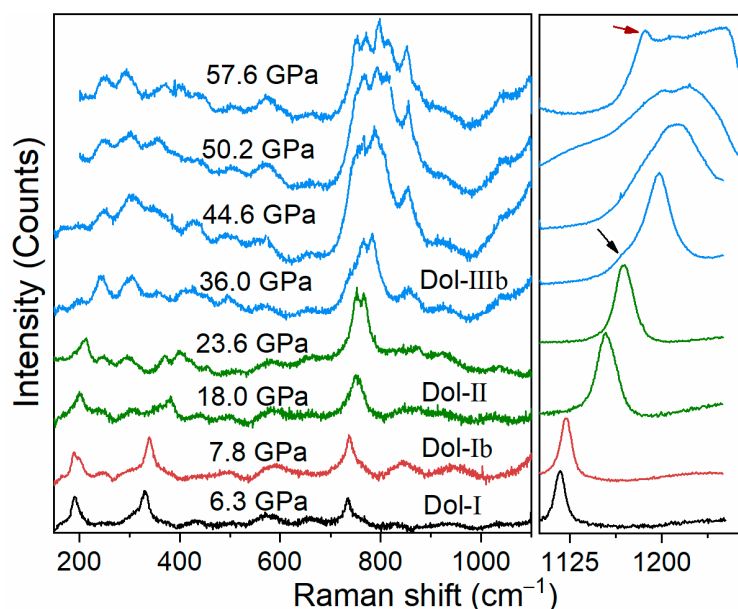

Figure 6. Representative Raman spectra of iron-bearing dolomite with increasing pressure. The Dol-Ib, Dol-II, and Dol-IIIb phases occur at around 7.8, 14.8 and 36.0 GPa, respectively. The new peak observed at 36.0 GPa (shown as the black arrow) represents the onset of Dol-IIIb phase. Meanwhile, one of the ν_1 modes shifts to a lower frequency of ~1186 cm^{-1} at 57.6 GPa (shown as the red arrow), which may be related to the 3 + 1 coordination in Dol-IIIb [29].

Furthermore, one of the ν_1 modes shifts to a lower frequency of ~1186 cm^{-1} at 57.6 GPa (shown as the red arrow in Figure 6). It may be related to the 3 + 1 coordination (three strong and one weaker C-O banding, more detailed information can refer to the reference therein) in dolomite-IIIb as illustrated by Raman spectroscopy on Ca$_{1.00}$Mg$_{0.92}$Fe$_{0.08}$(CO$_3$)$_2$ [29] and XRD results on CaMg$_{0.6}$Fe$_{0.4}$(CO$_3$)$_2$ [30]. The onset phase transition pressure of the 3 + 1 coordination observed in this study is about 8 GPa lower than that in Ca$_{1.00}$Mg$_{0.92}$Fe$_{0.08}$(CO$_3$)$_2$ [29], which may be attributed to either high iron content or the relatively large deviatoric stress induced by the argon pressure medium.

In this study, we observed the splitting and lower frequency of ν_1 modes in the dolomite-IIIb phase, unlike the splitting of the ν_1 modes into the two Raman peaks in siderite across the spin transition of iron (Figures 1 and 2). It suggests that there is no spin transition of iron in Ca$_{1.02}$Mg$_{0.76}$Fe$_{0.20}$Mn$_{0.02}$(CO$_3$)$_2$ up to 58 GPa. Moreover, the pressure-volume profiles of iron-rich dolomite CaMg$_{0.6}$Fe$_{0.4}$(CO$_3$)$_2$ show that there is no volume collapse observed at the whole pressure range of dolomite-IIIb phase [28,30], suggesting that no spin transition occurs at 36−115 GPa. By contrast, Mao et al. (2011) [27] put forward that the spin transition of Ca$_{0.988}$Mg$_{0.918}$Fe$_{0.078}$Mn$_{0.016}$(CO$_3$)$_2$ was at ~47 GPa with a volume collapse of 2% based on the compression and decompression XRD data. In addition, theoretical calculations have predicted a higher spin transition pressure of 65−68 GPa for iron-rich dolomite [51]. To eliminate such discrepancy, further experiments are imperative with more sensitive probes including synchrotron Mössbauer spectroscopy and X-ray emission spectroscopy.
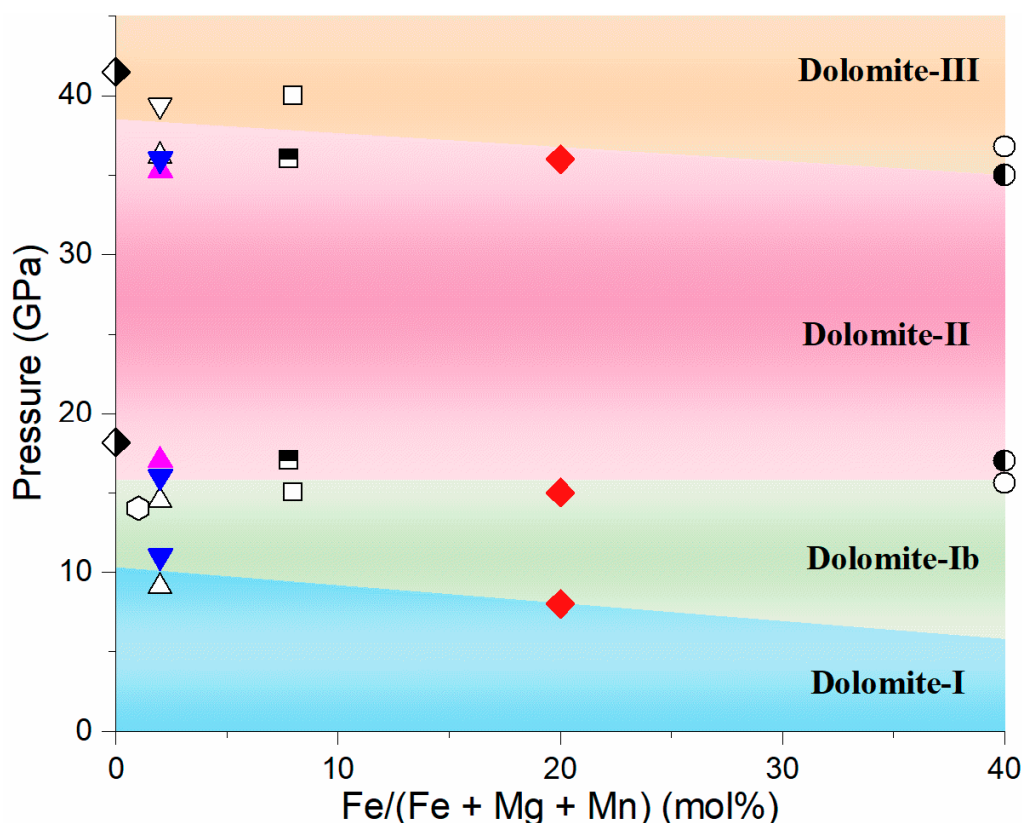

Figure 7. Phase transitions of dolomite as a function of iron content. The cyan, green, magenta, and yellow areas represent the dolomite-Ib, -II, -III phases. Solid red diamonds, ◆: Ca$_{1.02}$Mg$_{0.76}$Fe$_{0.20}$Mn$_{0.02}$(CO$_3$), this study; half open and half solid black diamonds, ◈: CaMg(CO$_3$)$_2$ [28]; open black hexagon, ⬡: Ca$_{1.001}$Mg$_{0.987}$Fe$_{0.01}$Mn$_{0.002}$(CO$_3$)$_2$ [52]; open black up triangles, △: CaMg$_{0.98}$Fe$_{0.02}$(CO$_3$)$_2$ [25]; open black down triangle, ▽: CaMg$_{0.98}$Fe$_{0.02}$(CO$_3$)$_2$ [24]; solid magenta triangles, ▲: CaMg$_{0.98}$Fe$_{0.02}$(CO$_3$)$_2$ [24]; half open and half solid black squares, ◪: Ca$_{0.988}$Mg$_{0.918}$Fe$_{0.078}$Mn$_{0.016}$(CO$_3$)$_2$ [27]; open black squares, □: CaMg$_{0.92}$Fe$_{0.08}$(CO$_3$)$_2$ [29]; open black circles, ○: CaMg$_{0.6}$Fe$_{0.4}$(CO$_3$)$_2$; half open and half solid black circles, ◑: CaMg$_{0.6}$Fe$_{0.4}$(CO$_3$)$_2$ [28].

Table 3. Overview of the current literature about dolomite and a comparison of the methods used, composition, and phase transition pressure.

Composition	Dol-Ib	Dol-II (P$\bar{1}$)	Dol-III (P$\bar{1}$)	Dol-IV (Pnma)	Dol-V (C2/c)	Methods	PTM	References
$Ca_{1.02}Mg_{0.76}Fe_{0.20}Mn_{0.02}(CO_3)$	8	15	36	-	-	Raman	Argon	This study
$CaMg_{0.6}Fe_{0.4}(CO_3)_2$	-	15.58	36.81 (IIIb) [a]	115.18 GPa and 2500 K	-	XRD	Ne	[28]
	-	17	35 (IIIb)	-	-	XRD	Ne	[30]
$CaMg_{0.92}Fe_{0.08}(CO_3)_2$	-	15	40	-	-	Raman	Ne	[29]
	-	-	-	-	-	XRD	MEW	[53]
	-	-	-	-	-	MIR	KBr	[53]
$Ca_{0.988}Mg_{0.918}Fe_{0.078}Mn_{0.016}(CO_3)_2$	-	17 [b]	36 [c]	45 GPa and 1500 K	-	XRD	Ne	[27]
$CaMg_{0.98}Fe_{0.02}(CO_3)_2$	-	-	-	-	46.2 GPa and 300 K [d]	XRD	Ne	[25]
	-	17	35.3	-	-	FIR	Petroleum jelly	[24]
	-		39.4	-	-	Raman	Ne	[24]
	9.1	14.5	36.2 (IIIc)	-	39.5 GPa, and 1880 K	Raman	Ne	[25]
	11	16	36 (IIIc)	-	-	Raman and MIR	Argon	[26]
$CaMg_{0.98}Fe_{0.01}Mn_{0.02}(CO_3)_2$	-	-	-	-	-	XRD	Silicone oil	[54]
	-	-	-	-	-	XRD	ME	[55]
$Ca_{1.001}Mg_{0.987}Fe_{0.01}Mn_{0.002}(CO_3)_2$	-	14	-	-	-	XRD	Ne	[52]
$CaMg(CO_3)_2$	-	-	43.4 (IIIc) [e]	-	43 GPa	DFT	n.a.	[25]
	-	18.16	41.5 (IIIc)	-	-	XRD	Ne	[28]
N/A	-	-	-	-	-	Raman	KBr	[56]
N/A	-	-	-	-	-	Raman	ME	[57]

[a] The space group of Dol-IIIb is R3. [b] The Dol-II is an orthorhombic phase. [c] The temperature is 1500 K, but not 300 K in this phase. [d] The phase is formed after 1800 K annealing. The phase transitions pressure and temperature of dolomite are in the unit of GPa and K, therein, the phase transition pressure of the Dol-Ib, Dol-II, Dol-III are at 300 K

4. Conclusions

Two iron-bearing carbonates, i.e., siderite and iron-bearing dolomite, were investigated by Raman spectroscopy at high pressure and room temperature in DACs using varying pressure media. The electronic spin-paring transition of iron in siderite occurs sharply at 42–44 GPa using helium as the pressure medium, while it is ~38–48 GPa in the NaCl pressure medium. It suggests that the spin crossover of siderite is significantly influenced by large deviatoric stress. Considering the high temperature environment of the Earth's interior, the stress field of the Earth's interior should be close to a hydrostatic environment, which is considered to be a factor for modeling carbon subduction at deep mantle conditions [24].

For iron-bearing dolomite, the high-pressure phase (dolomite-IIIb) can be stable at least to 58 GPa at room temperature. It is a potential carbon carrier and could carry carbon down to the deep mantle via cold subduction slabs [27,28,30]. In addition, based on the vibrational properties of iron-bearing dolomite in this study and high-pressure XRD results from Merlini et al. (2017) [28], there is no spin transition of iron in dolomite with iron content up to 40 mol% at high pressure from 36 to 115 GPa. Further investigation is needed to clarify the spin transition of iron in dolomite by using more sensitive probes (e.g., X-ray emission spectroscopy).

References

1. Shcheka, S.S.; Wiedenbeck, M.; Frost, D.J.; Keppler, H. Carbon solubility in mantle minerals. *Earth Planet. Sci. Lett.* **2006**, *245*, 730–742. [CrossRef]

2. Boulard, E.; Guyot, F.; Fiquet, G. High-pressure transformations and stability of ferromagnesite in the Earth's mantle. *Carbon Earth's Inter.* **2020**, 105–113. [CrossRef]

3. Hazen, R.M.; Downs, R.T.; Jones, A.P.; Kah, L. Carbon mineralogy and crystal chemistry. *Rev. Mineral. Geochem.* **2013**, *75*, 7–46. [CrossRef]

4. Hazen, R.M.; Schiffries, C.M. Why deep carbon? *Rev. Mineral. Geochem.* **2013**, *75*, 1–6. [CrossRef]

5. Brenker, F.E.; Vollmer, C.; Vincze, L.; Vekemans, B.; Szymanski, A.; Janssens, K.; Szaloki, I.; Nasdala, L.; Joswig, W.; Kaminsky, F. Carbonates from the lower part of transition zone or even the lower mantle. *Earth Planet. Sci. Lett.* **2007**, *260*, 1–9. [CrossRef]

6. Wang, A.; Pasteris, J.D.; Meyer, H.O.A.; Dele-Duboi, M.L. Magnesite-bearing inclusion assemblage in natural diamond. *Earth Planet. Sci. Lett.* **1996**, *141*, 293–306. [CrossRef]

7. Fu, S.; Yang, J.; Lin, J.F. Abnormal elasticity of single-crystal magnesiosiderite across the spin transition in Earth's lower mantle. *Phys. Rev. Lett.* **2017**, *118*, 036402. [CrossRef]

8. Gaillard, F.; Malki, M.; Iacono-Marziano, G.; Pichavant, M.; Scaillet, B. Carbonatite melts and electrical conductivity in the asthenosphere. *Science* **2008**, *322*, 1363–1365. [CrossRef]

9. Yao, C.; Wu, Z.; Zou, F.; Sun, W. Thermodynamic and elastic properties of magnesite at mantle conditions: First-principles calculations. *Geochem. Geophys. Geosystems* **2018**, *19*, 2719–2731. [CrossRef]

10. Liu, J.; Lin, J.F.; Mao, Z.; Prakapenka, V.B. Thermal equation of state and spin transition of magnesiosiderite at high pressure and temperature. *Am. Mineral.* **2014**, *99*, 84–93. [CrossRef]

11. Boulard, E.; Pan, D.; Galli, G.; Liu, Z.; Mao, W.L. Tetrahedrally coordinated carbonates in Earth's lower mantle. *Nat. Commun.* **2015**, *6*, 6311. [CrossRef] [PubMed]

12. Cerantola, V.; Wilke, M.; Kantor, I.; Ismailova, L.; Kupenko, I.; McCammon, C.; Pascarelli, S.; Dubrovinsky, L.S. Experimental investigation of $FeCO_3$ (siderite) stability in Earth's lower mantle using XANES spectroscopy. *Am. Mineral.* **2019**, *104*, 1083–1091. [CrossRef]

13. Liu, J.; Hu, Q.; Bi, W.; Yang, L.; Xiao, Y.; Chow, P.; Meng, Y.; Prakapenka, V.B.; Mao, H.K.; Mao, W.L. Altered chemistry of oxygen and iron under deep Earth conditions. *Nat. Commun.* **2019**, *10*, 153. [CrossRef] [PubMed]

14. Liu, J.; Wang, C.; Lv, C.; Su, X.; Tang, R.; Chen, J.; Hu, Q.; Mao, H.-K.; Mao, W. Evidence for oxygenation of Fe-Mg oxides at mid-mantle conditions and the rise of deep oxygen. *Natl. Sci. Rev.* **2020**, *1*, 1–6. [CrossRef]

15. Cerantola, V.; Bykova, E.; Kupenko, I.; Merlini, M.; Ismailova, L.; McCammon, C.; Bykov, M.; Chumakov, A.I.; Petitgirard, S.; Kantor, I.; et al. Stability of iron-bearing carbonates in the deep Earth's interior. *Nat. Commun.* **2017**, *8*, 15960. [CrossRef]

16. Liu, J.; Lin, J.F.; Prakapenka, V.B. High-pressure orthorhombic ferromagnesite as a potential deep-mantle carbon carrier. *Sci. Rep.* **2015**, *5*, 7640. [CrossRef]

17. Lavina, B.; Dera, P.; Downs, R.T.; Yang, W.; Sinogeikin, S.; Meng, Y.; Shen, G.; Schiferl, D. Structure of siderite $FeCO_3$ to 56 GPa and hysteresis of its spin-pairing transition. *Phys. Rev. B* **2010**, *82*, 064110. [CrossRef]

18. Lobanov, S.S.; Goncharov, A.F.; Litasov, K.D. Optical properties of siderite ($FeCO_3$) across the spin transition: Crossover to iron-rich carbonates in the lower mantle. *Am. Mineral.* **2015**, *100*, 1059–1064. [CrossRef]

19. Cerantola, V.; McCammon, C.; Kupenko, I.; Kantor, I.; Marini, C.; Wilke, M.; Ismailova, L.; Solopova, N.; Chumakov, A.; Pascarelli, S.; et al. High-pressure spectroscopic study of siderite ($FeCO_3$) with a focus on spin crossover. *Am. Mineral.* **2015**, *100*, 2670–2681. [CrossRef]

20. Lin, J.-F.; Liu, J.; Jacobs, C.; Prakapenka, V.B. Vibrational and elastic properties of ferromagnesite across the electronic spin-pairing transition of iron. *Am. Mineral.* **2012**, *97*, 583–591. [CrossRef]

21. Nagai, T.; Ishido, T.; Seto, Y.; Nishio-Hamane, D.; Sata, N.; Fujino, K. Pressure-induced spin transition in $FeCO_3$-siderite studied by X-ray diffraction measurements. *J. Phys. Conf. Ser.* **2010**, *215*, 012002. [CrossRef]

22. Spivak, A.; Solopova, N.; Cerantola, V.; Bykova, E.; Zakharchenko, E.; Dubrovinsky, L.; Litvin, Y. Raman study of $MgCO_3$–$FeCO_3$ carbonate solid solution at high pressures up to 55 GPa. *Phys. Chem. Miner.* **2014**, *41*, 633–638. [CrossRef]

23. Wei Chariton s, C.; Sternemann, C.; Cerantola, V.; Sahle, C.J.; Spiekermann, G.; Harder, M.; Forov, Y.; Kononov, A.; Sakrowski, R.; Yavas, H.; et al. Pressure driven spin transition in siderite and magnesiosiderite single crystals. *Sci. Rep.* **2017**, *7*, 16526.

24. Efthimiopoulos, I.; Germer, M.; Jahn, S.; Harms, M.; Reichmann, H.J.; Speziale, S.; Schade, U.; Sieber, M.; Koch-Müller, M. Effects of hydrostaticy on the structural stability of carbonates at lower mantle pressures: The case study of dolomite. *High Press. Res.* **2018**, *39*, 1–14. [CrossRef]

25. Binck, J.; Chariton, S.; Stekiel, M.; Bayarjargal, L.; Morgenroth, W.; Milman, V.; Dubrovinsky, L.; Winkler, B. High-pressure, high-temperature phase stability of iron-poor dolomite and the structures of dolomite-IIIc and dolomite-V. *Phys. Earth Planet. Inter.* **2020**, *299*, 106403. [CrossRef]

26. Efthimiopoulos, I.; Jahn, S.; Kuras, A.; Schade, U.; Koch-Müller, M. Combined high-pressure and high-temperature vibrational studies of dolomite: Phase diagram and evidence of a new distorted modification. *Phys. Chem. Miner.* **2017**, *44*, 465–476. [CrossRef]

27. Mao, Z.; Armentrout, M.; Rainey, E.; Manning, C.E.; Dera, P.; Prakapenka, V.B.; Kavner, A. Dolomite III: A new candidate lower mantle carbonate. *Geophys. Res. Lett.* **2011**, *38*, L22303. [CrossRef]

28. Merlini, M.; Cerantola, V.; Gatta, G.D.; Gemmi, M.; Hanfland, M.; Kupenko, I.; Lotti, P.; Müller, H.; Zhang, L. Dolomite-IV: Candidate structure for a carbonate in the Earth's lower mantle. *Am. Mineral.* **2017**, *102*, 1763–1766. [CrossRef]

29. Vennari, C.E.; Williams, Q. A novel carbon bonding environment in deep mantle high-pressure dolomite. *Am. Mineral.* **2018**, *103*, 171–174. [CrossRef]

30. Merlini, M.; Crichton, W.A.; Hanfland, M.; Gemmi, M.; Muller, H.; Kupenko, I.; Dubrovinsky, L. Structures of dolomite at ultrahigh pressure and their influence on the deep carbon cycle. *Proc. Natl. Acad. Sci. USA* **2012**, *109*, 13509–13514. [CrossRef]

31. Farsang, S.; Facq, S.; Redfern, S.A. Raman modes of carbonate minerals as pressure and temperature gauges up to 6 GPa and 500 °C. *Am. Mineral. J. Earth Planet. Mater.* **2018**, *103*, 1988–1998.

32. Klotz, S.; Chervin, J.C.; Munsch, P.; Le Marchand, G. Hydrostatic limits of 11 pressure transmitting media. *J. Phys. D Appl. Phys.* **2009**, *42*, 075413. [CrossRef]

33. Zhao, C.S.; Lv, C.J.; Xu, L.X.; Liu, J. Raman signatures of the distortion and stability of MgCO$_3$ to 75 GPa. *Am. Mineral.* **2021**, *106*. in press. [CrossRef]

34. Shen, G.; Wang, Y.; Dewaele, A.; Wu, C.; Fratanduono, D.E.; Eggert, J.; Klotz, S.; Dziubek, K.F.; Loubeyre, P.; Fat'yanov, O.V.; et al. Toward an international practical pressure scale: A proposal for an IPPS ruby gauge (IPPS-Ruby2020). *High Press. Res.* **2020**, *40*, 299–314. [CrossRef]

35. Mao, H.; Xu, J.-A.; Bell, P. Calibration of the ruby pressure gauge to 800 kbar under quasi-hydrostatic conditions. *J. Geophys. Res. Solid Earth* **1986**, *91*, 4673–4676. [CrossRef]

36. Rividi, N.; van Zuilen, M.; Philippot, P.; Menez, B.; Godard, G.; Poidatz, E. Calibration of carbonate composition using micro-Raman analysis: Application to planetary surface exploration. *Astrobiology* **2010**, *10*, 293–309. [CrossRef]

37. Boulard, E.; Guyot, F.; Fiquet, G. The influence on Fe content on Raman spectra and unit cell parameters of magnesite–siderite solid solutions. *Phys. Chem. Miner.* **2012**, *39*, 239–246. [CrossRef]

38. Lavina, B.; Dera, P.; Downs, R.T.; Prakapenka, V.; Rivers, M.; Sutton, S.; Nicol, M. Siderite at lower mantle conditions and the effects of the pressure-induced spin-pairing transition. *Geophys. Res. Lett.* **2009**, *36*, L23306. [CrossRef]

39. Farfan, G.; Wang, S.; Ma, H.; Caracas, R.; Mao, W.L. Bonding and structural changes in siderite at high pressure. *Am. Mineral.* **2012**, *97*, 1421–1426. [CrossRef]

40. Müller, J.; Speziale, S.; Efthimiopoulos, I.; Jahn, S.; Koch-Müller, M. Raman spectroscopy of siderite at high pressure: Evidence for a sharp spin transition. *Am. Mineral.* **2016**, *101*, 2638–2644. [CrossRef]

41. Santamaría-Pérez, D.; Gracia, L.; Garbarino, G.; Beltrán, A.; Chuliá-Jordán, R.; Gomis, O.; Errandonea, D.; Ferrer-Roca, C.; Martínez-García, D.; Segura, A. High-pressure study of the behavior of mineral barite by x-ray diffraction. *Phys. Rev. B* **2011**, *84*, 054102. [CrossRef]

42. Zhao, C.S.; Li, H.P.; Jiang, J.J.; He, Y.; Liang, W. Phase transition and vibration properties of MnCO$_3$ at high pressure and high-temperature by Raman spectroscopy. *High Press. Res.* **2018**, *38*, 212–223. [CrossRef]

43. Chariton, S.; McCammon, C.; Vasiukov, D.M.; Stekiel, M.; Kantor, A.; Cerantola, V.; Kupenko, I.; Fedotenko, T.; Koemets, E.; Hanfland, M.; et al. Seismic detectability of carbonates in the deep Earth: A nuclear inelastic scattering study. *Am. Mineral.* **2020**, *105*, 325–332.

44. Stekiel, M.; Nguyen-Thanh, T.; Chariton, S.; McCammon, C.; Bosak, A.; Morgenroth, W.; Milman, V.; Refson, K.; Winkler, B. High pressure elasticity of FeCO$_3$-MgCO$_3$ carbonates. *Phys. Earth Planet. Inter.* **2017**, *271*, 57–63. [CrossRef]

45. Hsu, H.; Huang, S.-C. Spin crossover and hyperfine interactions of iron in (Mg,Fe)CO$_3$ ferromagnesite. *Phys. Rev. B* **2016**, *94*, 060404. [CrossRef]

46. Mattila, A.; Pylkkänen, T.; Rueff, J.P.; Huotari, S.; Vankó, G.; Hanfland, M.; Lehtinen, M.; Hämäläinen, K. Pressure induced magnetic transition in siderite FeCO$_3$ studied by x-ray emission spectroscopy. *J. Phys. Condens. Matter* **2007**, *19*, 386206. [CrossRef]

47. Chao, K.-H.; Hsieh, W.-P. Thermal conductivity anomaly in (Fe$_{0.78}$Mg$_{0.22}$)CO$_3$ siderite across spin transition of iron. *J. Geophys. Res. Solid Earth* **2019**, *124*, 1388–1396. [CrossRef]

48. Boulard, E.; Menguy, N.; Auzende, A.L.; Benzerara, K.; Bureau, H.; Antonangeli, D.; Corgne, A.; Morard, G.; Siebert, J.; Perrillat, J.P.; et al. Experimental investigation of the stability of Fe-rich carbonates in the lower mantle. *J. Geophys. Res. Solid Earth* **2012**, *117*, B02208. [CrossRef]

49. Tsuchiya, J.; Nishida, R.; Tsuchiya, T. First Principles calculation of the stability of iron bearing carbonates at high pressure conditions. *Minerals* **2020**, *10*, 54. [CrossRef]

50. Williams, Q.; Collerson, B.; Knittle, E. Vibrational spectra of magnesite (MgCO$_3$) and calcite-III at high pressures. *Am. Mineral.* **1992**, *77*, 1158–1165.

51. Solomatova, N.V.; Asimow, P.D. First-principles calculations of high-pressure iron-bearing monoclinic dolomite and single-cation carbonates with internally consistent Hubbard U. *Phys. Chem. Miner.* **2017**, *45*, 293–302. [CrossRef]

52. Zucchini, A.; Prencipe, M.; Belmonte, D.; Paola, C. Ab initio study of the dolomite to dolomite-II high pressure phase transition. *Eur. J. Mineral.* **2017**, *29*, 227–238. [CrossRef]

53. Santillán, J.; Williams, Q.; Knittle, E. Dolomite-II: A high-pressure polymorph of CaMg(CO$_3$)$_2$. *Geophys. Res. Lett.* **2003**, *30*. [CrossRef]

54. Fiquet, G.; Guyot, F.; Itie, J.-P. High-pressure X-ray diffraction study of carbonates MgCO$_3$, CaMg(CO$_3$)$_2$, and CaCO$_3$. *Am. Mineral.* **1994**, *79*, 15–23.

55. Ross, N.L.; Reeder, R.J. High-pressure structural study of dolomite and ankerite. *Am. Mineral.* **1992**, *77*, 412–421.

56. Gillet, P.; Biellmann, C.; Reynard, B.; McMillan, P. Raman spectroscopic studies of carbonates part I: High-pressure and high-temperature behaviour of calcite, magnesite, dolomite and aragonite. *Phys. Chem. Miner.* **1993**, *20*, 1–18. [CrossRef]

57. Kraft, S.; Knittle, E.; Williams, Q. Carbonate stability in the Earth's mantle: A vibrational spectroscopic study of aragonite and dolomite at high pressures and temperatures. *J. Geophys. Res.* **1991**, *96*, 17997. [CrossRef]